Kinetic Mobility and Connectivity in Nanopore Networks

Fu Yang Wang, Zhong Hua Zhu, Paul Massarotto, and Victor Rudolph
School of Chemical Engineering, The University of Queensland, Brisbane, Qld 4072, Australia

DOI 10.1002/aic.12587
Published online March 8, 2011 in Wiley Online Library (wileyonlinelibrary.com).

Experimental results for methane and carbon dioxide diffusion in coal, as reported in the literature, often lead to diffusion rates of CO_2 appearing to be much greater than that of CH_4. The interpretation sometimes offered that the diffusion coefficient for CO_2 is 1–2 orders of magnitude higher than that of CH_4, violates fundamental principles. Nevertheless, the experimental observations require explanation. In this article, we: (a) Develop simplified models for the fast estimation of transport coefficients. These are compared with comprehensive grand canonical Monte Carlo (GCMC) and molecular dynamic (MD) simulations, collectively defined as molecular simulations (MS), which provide theoretical adsorption isotherms and various transport coefficients based on multicenter potential energy equations. The simplified models are shown to have acceptable accuracies. (b) Use the simplified models to compare diffusivities of CO_2 and CH_4 in carbon nanopores. For all cases examined, the diffusivity of CH_4 is always larger than that of CO_2. (c) Offer two explanations for the apparently contradictory experimental observations (that CO_2 sometimes appears to diffuse much faster than the CH_4 molecule, even though CH_4 is lighter and has smaller adsorption affinity): (i) CH_4 mobility could be significantly reduced by directional forces resulting from irregular pore geometries; and (ii) if pores contain throats with sizes close to the CH_4 molecular diameter, the energy barrier that the methane molecules must overcome to proceed through is much larger than that required for CO_2. (d) Demonstrate that both mobility and connectivity issues can be addressed using kinetic theory in association with percolation analysis. Furthermore, this method of understanding pore networks provides a number of important quantitative measures including percolation threshold, size of largest cluster, shortest path and tortuosity. Separating different transport mechanisms, as we propose here, provides improved insights into the complex transport phenomena that occur in carbonaceous porous media. In many cases, diffusivities reported in the literature with mixed mechanisms are better named "apparent transport coefficients," because they lump in other unrelated phenomena, violating the fundamental basis of, or mathematical assumptions imposed on, the definition of diffusion. *AIChE J*, 58: 364–376, 2012
Keywords: adsorption/gas, coal, diffusion (micropores), molecular simulation, percolation, porous media

Introduction

Accurate estimation of adsorption isotherms and diffusion coefficients of gases in porous media is essential for the prediction and optimization of the performance of various

Correspondence concerning this article should be addressed to Z. H. Zhu at z.zhu@uq.edu.au.

adsorption-diffusion separation processes. Application examples, which motivated this study, include CO_2 sequestration in deep coals associated with enhanced coal-bed methane operations, and CO_2—CH_4 separations using carbon nanotubes (CNTs). In both cases, the performance measured by methane recovery and CO_2—CH_4 selectivity depends on the adsorption affinities and transport coefficients of CO_2 and CH_4 in carbon nanopores.

Because of the practical significance of this area of work, there is an extensive literature, revealing somewhat contradictory evidence. A typical example is the transport of CO_2 and CH_4 in coals, where influential researchers report that the diffusivity of CO_2 in coals could be one to two orders of magnitude larger than that of CH_4.[1–3] These research results, based on experimental observations, and their subsequent interpretations, have been accepted and followed up in many subsequent works. However, it is well established from fundamental theory supported by many numerical simulations that CH_4 has a higher diffusion coefficient than CO_2.

We have previously shown that the experimental observations in which CO_2 apparently diffuses more quickly than CH_4 can be explained, in a manner qualitatively consistent with the fundamental theory.[4,5] Two major limitations in our previous works are a lack of molecular level studies, which limits the opportunity for insights at microscales, and a relatively cursory analysis of the pore network, including accessibility and connectivity.

In this article, we first develop simplified models for the fast estimation of transport coefficients. The basis for these is comprehensive molecular simulations using both GCMC and equilibrium molecular dynamic (EMD) algorithms described by Bhatia and Nicholson,[6,7] which are applied for the determination of adsorption isotherms and transport properties of CO_2 and CH_4 in slit-shaped, graphite nanopores under various conditions. In the computation of potential energies, a multicenter computational strategy described by Potoff and Siepmann[8] as well as Do and Do[9,10] accounting for interactions among atoms and electrical charges is used to replace the more usual hard-sphere potential energy models. Solid-fluid and fluid-fluid atomic interactions are quantified by the Steele[11] 10-4-3 and the Lennard-Jones (L-J)[8,12] 12-6 potential energy equations. Interactions among electrical charges are computed using Coulomb's law. The fugacity is used in both GCMC and EMD simulation. The fugacity values are converted to pressures using cubic equations of state.[12] We have tested four cubic equations of state, namely, van der Waals, Redlich-Kwong, Soave, and Peng-Robinson with similar results. Pressures reported in this article are computed using the Redlich-Kwong equation of state for the consistency.

Using the referenced molecular simulations, we develop some more tractable models for the fast estimation of the transport coefficients, avoiding further reliance on the rather time-consuming MS methods. The results from these models indicate that the diffusion coefficients of CH_4 are notably larger than that of CO_2 under a broad range of operational conditions, as fundamentally expected, but in general contradiction to a number of publications in the coal literature.[1–3]

It is consequently necessary to investigate and explain the possible reasons leading to faster CO_2 transport in graphite nanopores than CH_4, even though the magnitudes of diffusion coefficients suggest that the opposite should occur. This is done in the second part of the article.

An examination of the kinetic mobility and the connectivity of the nanopore networks provide physical insights that explain the contradictory results reported in the literature. Carbon dioxide molecules have an elongated shape with minor and major axes about 3 and 6 Å, respectively, compared with a roughly spherical methane molecule, which has a L-J collision diameter of 3.76 Å. For pores only slightly larger than methane, the transport energy barrier for CO_2 is much lower than that of CH_4. This leads to higher activated transport coefficients of CO_2 as a result of relatively lower energy barrier. The reason leading to different energy barriers are that elongated CO_2 molecules adopt a configuration parallel to the walls to achieve minimum free energy, whereas large repulsive forces are imposed on CH_4 molecules due to their closer proximity with the pore walls.

This accessibility is conceptually different from diffusivity, which should be quantified separately from the diffusion processes. An "overall diffusion coefficient" that incorporates activation energies at boundaries violates the continuity condition, which is implicit in the diffusion equations. In addition to this continuity requirement, the traditional Fick and Einstein diffusion equations deal with molecular transport in random force fields. However, as we have demonstrated previously, directional forces can be generated by irregular nanopore geometries and surface chemistries.[13] In these cases, the Fick or Einstein form of the diffusion equation must be replaced by the more complete Smoluchowski or Fokker-Planck equation. An example is provided in the article to demonstrate that under certain conditions, the directional forces may impose much stronger effect on the transport of CH_4 compared with that of CO_2 molecules. For situations where directional force fields are important, diffusion coefficients obtained using Fick and Einstein diffusion equations are incorrect and misleading.

Since there may be substantial differences between entrance activation energies and directional forces acting on CO_2 and CH_4 molecules in nanopores, it may be deduced that some pores that are available for CO_2 transport could be inactive for CH_4 transport. Consequently, pore network connectivity is proposed as the explanation for the unexpected experimental observations regarding the magnitudes of CH_4 and CO_2 diffusion coefficients in coal.

The pore network connectivity is analyzed using percolation theory. Percolation theory and related topics make an important contribution to porous media research, as witnessed by a number of full-length books,[14,15] and books with percolation theory as a core topic.[16,17] Percolation theory has been successfully applied to the fluid flow through fractured solids,[16,17] analysis of H1 and H2 type adsorption hysteresis with capillary condensation,[18,19] binary gas separation using membranes,[20] hydrogeology with scale-dependent hydraulic conductivity,[15,21,22] and quantum computation.[23]

A graph theory approach to percolation analysis is described in the article for the study of small pore networks. Typical networks commonly encountered in engineering applications are developed and analyzed using the graph theory to obtain key network properties including percolation threshold, spanned clusters, shortest path, and tortuosity. It can be demonstrated that under certain conditions, such as in

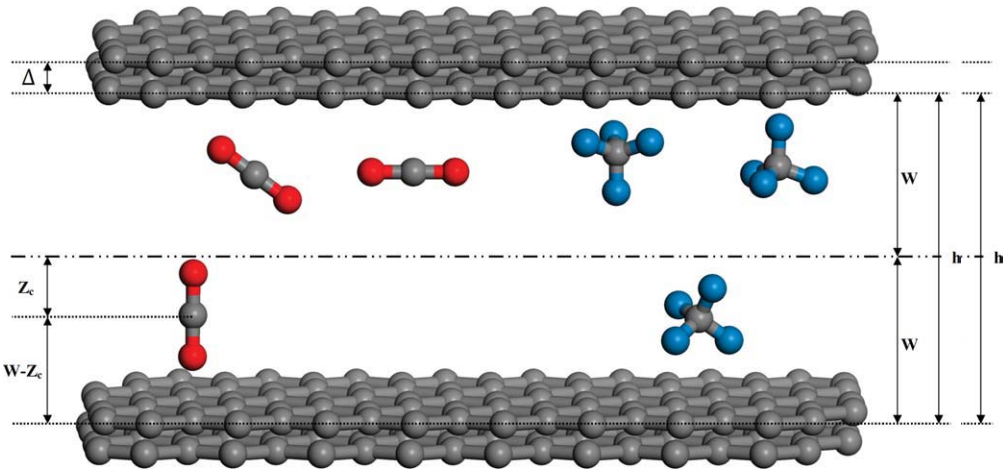

Figure 1. CO_2 and CH_4 configurations in slit-shaped graphite pore.

[Color figure can be viewed in the online issue, which is available at wileyonlinelibrary.com.]

networks where there are a significant number of throats with the size close to 3.7 Å, and/or cone shaped pores in the size range 8–10 Å, the network connectivity for CH_4 can be markedly lower than that of CO_2, providing reduced effective porosity, increased transport path lengths and tortuosity for CH_4. If the probability of connected pores is only slightly larger than the percolation threshold, a very small CH_4 flux is predicted; in some cases the ratio of the apparent transport coefficients of CO_2 to CH_4 can approach infinity when the connectivity for CO_2 is greater than the percolation threshold whereas that for CH_4 is not.

An aggregated apparent transport coefficient, which incorporates many mechanisms, should not be confused with diffusivity. The experimental observations can be explained by addressing separately diffusion in the ordered force field, kinetic mobility, and connectivity, without violating any fundamental considerations. All of these separate issues can be addressed simultaneously within the framework of molecular transport through nanopore networks.

Multicenter Potential Model and Adsorption Isotherms

The computation of various potential energies is necessary for the determination of adsorption isotherms and transport coefficients. Two most important parameters for the computation of potential energies are the L-J collision diameter σ and the ratio between the characteristic energy ε and Boltzmann constant k_B, namely ε/k_B. Due to complexities arising from its structure, broad ranges of these two parameters have been reported for CO_2 with $\sigma = 3.3 - 3.996$ Å and $\varepsilon/k_B = 190.0 - 246.2$ K. The various possible orientations of CO_2 molecules in nanopores most likely explain these observed ranges. Consequently, the hard sphere molecular model is inadequate and the multicenter model, which has the ability to quantify interactions between atoms should be used.[8–10,24]

Configurations of multicentered CO_2 and CH_4 molecules in a slit-shaped, graphite pore are schematically presented in Figure 1, in which three and four ball-and-stick atom molecules represent CO_2 and CH_4, respectively. Figure 1 shows the shape of a CO_2 molecule consisting of three atoms is linear, and this can hardly be represented as a hard sphere without introducing significant errors. The hard sphere approximation works better for CH_4 molecules but even these are not perfectly spherical, and are better represented by a multicenter model. For technical consistency, multicenter models for both CO_2 and CH_4 are used in this work. Dimensions indicated in the figure are used in the molecular simulations.

The parameters of CO_2 and CH_4 molecules used in the molecular simulations are listed in Table 1. Multicenter models are used in almost all simulations. The single center model with L-J parameters of CO_2 and CH_4 provided in Table 1 is only used in the demonstration of the Smoluchowski diffusion equation, which will be clearly indicated later in the relevant section. The TraPPE force field (nonpolarizable all-atom transferable potentials for phase equilibrium) is assumed in the multicenter models. The O=C bond length and the C—H bond length are specified as 1.16 and 1.087 Å, respectively. In Table 1, the unit e is used for the quantification of electrical charge q with the definition as $1\ e = 1.602 \times 10^{-19}$ Coulombs. The temperature used in all simulations is 300 K.

The parameters of the graphite wall are listed in Table 2, in which Δ and ρ_s denote the spacing of lattice layers and the lattice number density, respectively.

Table 1. Parameters of CO_2 and CH_4

Site	σ (Å)	ε/k (K)	q (e)	Reference
C in CO_2	2.8	27	+0.7	8
C in CH_4	3.4	55.055	−0.464	25,26
O in CO_2	3.05	79	−0.35	8
H in CH_4	2.65	7.901	+0.116	25,26
CO_2	3.454	235.9		27
CH_4	3.780	154		28

Table 2. Parameters of Graphite

Pore Type	σ (Å)	ε/k (K)	Δ (Å)	ρ_s (1/nm^3)	Reference
Slit Pore	3.4	28	3.35	114	11

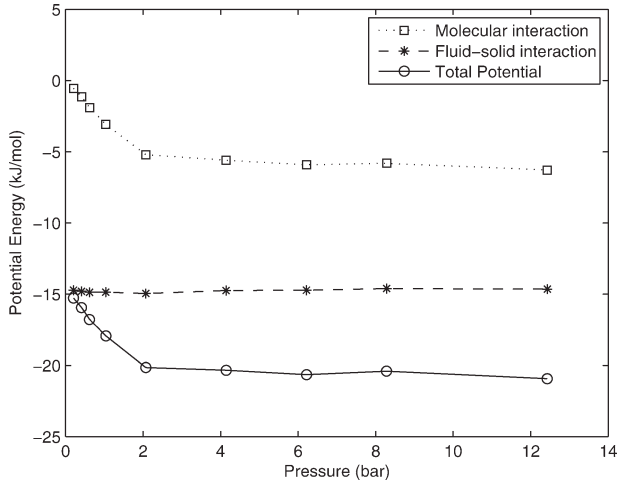

Figure 2. Average potential energy profiles of CO_2 in 1 nm graphite pore from MD simulations.

Besides parameters specified in Tables 1 and 2, the molecular simulations use the Steele[11] 10-4-3 and the L-J[8,12] 12-6 potential energy equations for solid-fluid and fluid-fluid atomic interactions, and Coulomb's law for electrical charge interactions.

In GCMC simulations, the wall area is chosen as $5 \times 5 = 25$ nm^2, leading to the total volume of the simulation cell as $25 \times h$ nm^3, where h is the pore width. The number of molecules in the simulation cell change with pressures and gas species, ranging from a few molecules to several hundreds. Both number of cycles and frequency of statistical data collection are specified as 10^5. Through the GCMC simulations, three potential energy profiles in nanopores vs. pressures can be determined for specified pore sizes, namely molecular interaction energy, fluid-solid interaction energy, and total energy. Representative curves of average potential energy profiles are shown in Figure 2 for CO_2 in a I nm graphite pore. In the figures presented in this article, results from GCMC and MD simulations are normally represented by symbols connected by lines to show the trend, and predictions using the simplified models are depicted by smooth curves. Absolute pressures are used in all illustrations. The pore size is defined as the distance from the center of the first carbon layer in one wall to the center of the first carbon layer in the opposite wall denoted as h in Figure 1. Due to the symmetric feature of slit pores, the half pore width denoted by w shown in Figure 1 is commonly used in simulations and representations.

It can be seen from Figure 2 that fluid-solid interaction energy hardly changes with pressure. Both molecular interaction energy and total potential energy change in the low pressure range 0–2 bar (abs), but not for higher values. The profiles shown in Figure 2 are useful for the development of simplified tractable models.

The MS results for adsorption isotherms of CO_2 and CH_4 in a 1 nm pore at 300 K are depicted in Figure 3. This shows that over a very broad pressure range, the adsorption isotherm of CH_4 is nearly linear, that is, follows Henry's law, whereas a linear approximation for CO_2 adsorption is restricted to the range of 0–2 bar.

The Boltzmann factor is commonly used to estimate the pore density in nanopores under low pressure. It is valid in the linear Henry's law adsorption regime. We will show in this work that even in the nonlinear regime, the Boltzmann factor still provides reasonable estimation of the pore density of CO_2 using the total potential in place of the fluid-solid potential energy.

The point-wise density $\rho(\mathbf{r})$ and average density $\hat{\rho}$ are estimated by Boltzmann factor under low pressure as follows:

$$\begin{aligned} \rho(\mathbf{r}) &= \rho_g \exp\left[-\frac{\Phi(\mathbf{r})}{k_B T}\right] \\ \hat{\rho} &= \frac{\rho_g}{V}\int \exp\left[-\frac{\Phi(\mathbf{r})}{k_B T}\right] d\mathbf{r} \end{aligned} \tag{1}$$

where Φ is the potential energy, T is the temperature, ρ_g is the bulk phase gas density, $\mathbf{r}$ is the vector of the spatial coordinate, and V is the volume in which the average value is computed. The mathematical representation of V is the integration of d$\mathbf{r}$ ($V = \int d\mathbf{r}$). For one-dimensional systems, volume V and vector $\mathbf{r}$ are replaced by length L and scalar r, respectively. If the total potential energy is used, the Boltzmann factor can be applied to relatively high pressures with reasonable accuracy. This extension will be validated later in the diffusivity computations.

Diffusion Coefficients

In this article, the scientific terms of "diffusion coefficient" and "diffusivity" are defined equally.[12] The computation of diffusion coefficients using equilibrium MD (EMD) simulations follows the theoretical derivations described by Bhatia and Nicholson.[6,7] The size of the simulation cell is the same as GCMC simulations as explained in the previous section. The number of time steps and frequency of statistical data collection are both set to 10^6. The total diffusivity (D_t) consists of self diffusivity (D_s) and viscous contributions to the diffusivity (D_v), that is, $D_t = D_s + D_v$. Total diffusivity profiles of CO_2 and CH_4 as functions of pressures at 300 K in 1 nm pores obtained from EMD simulations are given in Figure 4, which shows that: (1) the diffusivity of CH_4 is

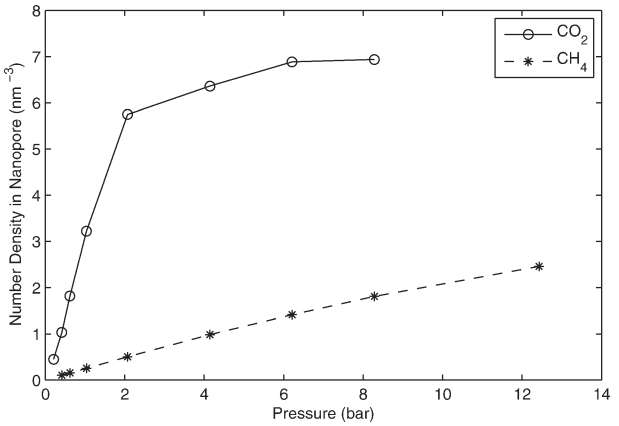

Figure 3. Theoretical adsorption isotherms of CO_2 and CH_4 in 1 nm graphite pore from GCMC simulations.

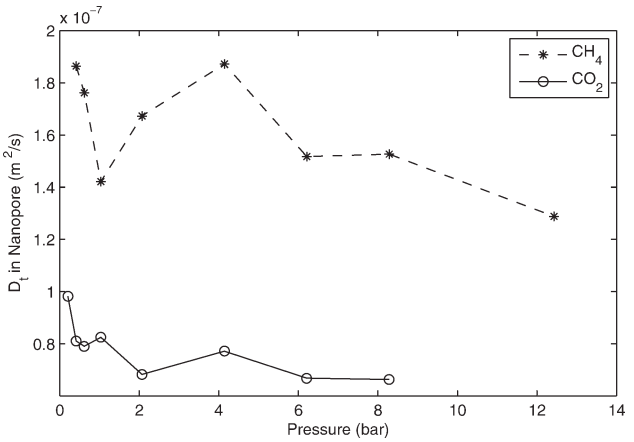

Figure 4. Total diffusivity variations with pressure for CO_2 and CH_4 in 1 nm graphite pore from MD simulations.

about twice that of CO_2; and (2) the diffusivities of both CO_2 and CH_4 decrease with increasing pressure. The oscillations in the diffusivity values, most obviously for CH_4 under low pressure, reflect our use of a relatively low value (10^6) for the number of time steps, to reduce computing times. The profiles could be improved (i.e., smoothed) by increasing the number of time steps.

Under low pressure (0.207 bar) and specified temperature (300 K), the diffusivities of both CO_2 and CH_4 increase with increasing pore widths as shown in Figure 5, for pores under 1 nm. Under all conditions in our equilibrium MD simulations, CH_4 diffusivity is always above CO_2 without any exception. The minimum difference between CH_4 and CO_2 diffusivity occurs at pore width $h = 0.72$ nm, the minimum width for CH_4 transport. (The pore width is given as the C atom center-to-center distance between the graphite walls, so the width available for the methane molecule is $0.72 - 0.34 = 0.38$ nm.) The interpretation frequently reported in the coal literature that CO_2 has diffusivity significantly larger than CH_4 is fundamentally incorrect and not supported by MD simulations.

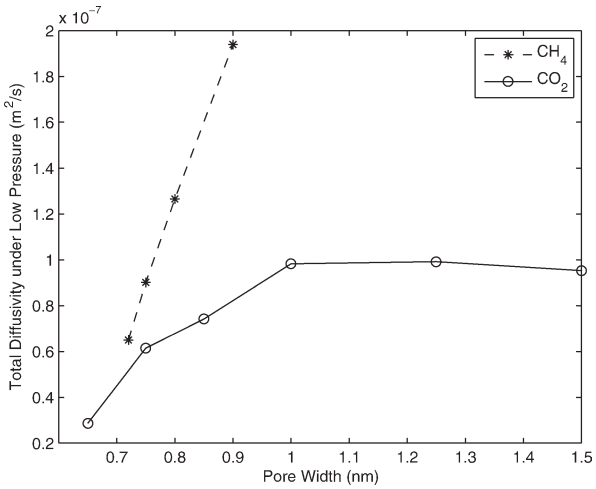

Figure 5. Diffusivity variation with pore width for CO_2 and CH_4 at 0.207 bar from MD simulations.

We have previously proposed tractable models[24] for the estimation of various diffusion coefficients, without resorting to MD simulations, by extending the work reported by Jepps and Bhatia.[29] These models are further refined here.

Both the self diffusivity model and the viscous model require the potential energy distribution profile in nanopores, which is shown in Figure 6 using CO_2 in 1.4 nm nanopore as an example for the determination of the notations $\Phi(0)$ and z_0. In our previous work,[24] the self diffusivity, also known as the boundary reflection term, denoted by D_s, was represented using the integral mean value as follows:

$$\begin{aligned} D_s(w) &= \frac{k_B T}{\widehat{\rho}\, w}\left[\frac{1}{k\rho_0}\left(\int_0^{z_0}\rho(\xi)\,d\xi\right)^2\right] \\ &= \frac{k_B T z_0^2}{kw}\exp\left[\frac{\Phi(w_m,w)+\Phi(z_0,w)-2\Phi(z_{m0},w)}{k_B T}\right] \\ &= \frac{k_B T z_0^2}{kw}\exp\left(-\frac{E_b}{k_B T}\right) \\ k &= \sqrt{\frac{m k_B T}{2\pi}} \\ E_b &= |\Phi(w_m,w)+\Phi(z_0,w)-2\Phi(z_{m0},w)| \end{aligned} \tag{2}$$

In Eq. 2, Φ is the potential energy, z_0 is the position related to minimum potential energy shown in Figure 6, w_m and z_{m0} are median points in integral mean value theory, which can be determined numerically using the following equations:

$$\begin{aligned} \hat{\rho}(w) &= \frac{\rho_\infty}{w}\int_0^w \exp\left[-\frac{\Phi(z,w)}{k_B T}\right]dz \\ &= \rho_\infty \exp\left[-\frac{\Phi(w_m)}{k_B T}\right];\ 0 \le w_m \le w \\ \int_0^{z_0}\rho(z,w)\,dz &= z_0\rho_\infty \exp\left[-\frac{\Phi(z_{m0},w)}{k_B T}\right];\ 0 \le z_{m0} \le z_0 \end{aligned} \tag{3}$$

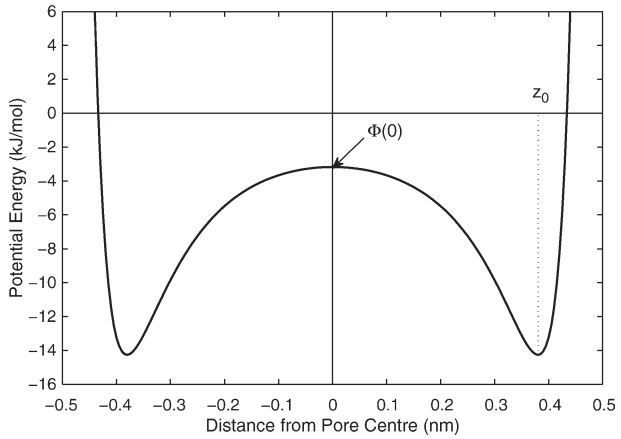

Figure 6. Representative potential energy profile of CO_2 in 1.4 nm graphite pore from GCMC simulation.

The disadvantage of Eq. 2 is that it can only be applied to processes under low pressures, and the activation energy E_b is quite different from traditionally accepted activation energy. These two limitations can be removed by using the total potential energy instead of fluid-solid interaction energy only, and restructuring the model as follows:

$$\begin{aligned} D_s(w;p) &= \frac{k_B T z_0^2}{kw}\exp\left[\frac{\Phi(z_0,w;p)}{k_B T}\right] \\ &\quad\times\exp\left[\frac{\Phi(w_m,w;p)-2\Phi(z_{m0},w;p)}{k_B T}\right] \\ &= \left\{\frac{k_B T z_0^2}{kw}\exp\left[\frac{\Phi(z_0,w;p)}{k_B T}\right]\right\}\exp\left(-\frac{E_s(w;p)}{k_B T}\right) \\ E_s &= \Phi(w_m,w;p)-2\Phi(z_{m0},w;p) \end{aligned} \tag{4}$$

Equation 4 reveals that the self diffusivity is pressure dependent, which is consistent with MD simulations. It can be seen that Eq. 4 is structurally similar to a previously reported surface diffusivity model given by:[5,30]

$$D_\mu(w) = D^0_{\mu,\infty}\exp\left[-\frac{aE(w)}{RT}\right] \tag{5}$$

With the incorporation of pressure effects and the removal of the empirical parameters, Eq. 4 represents an advance on previous models with an added advantage of providing clearer physical insights regarding the origin and meaning of the terms.

We now modify the viscous model given by:[24,29]

$$\begin{aligned} D_v &= \frac{k_B T}{\widehat{\rho}\, w}\int_0^{z_0}\frac{1}{\eta(z;p)}\left(\int_0^z \rho(\xi;w;p)\,d\xi\right)^2 dz \\ &\approx \frac{k_B T \rho_g^2}{\widehat{\rho}\, w}\int_0^{z_0}\frac{1}{\eta(z;p)}\left(\int_0^z \exp\left[-\frac{\Phi(\xi,w;p)}{k_B T}\right]d\xi\right)^2 dz \end{aligned} \tag{6}$$

Since Eq. 6 consists of double integration with an implicit function Φ, it is not easy to solve. However, through inspection of Figure 6, it can be seen that the potential curve in the section [0 z_0] can be approximated by a parabolic function $\Phi(z) = az^2 + b$ with parameters "a" and "b" both negative. For example, for CO_2 under low pressure in 1 nm graphite pore, we have $a = -265.39$ kJ/(mol nm^2), $b = -12.89$ kJ/mol; these become $a = -75.146$ kJ/(mol nm^2) and $b = -3.172$ kJ/mol in 1.5 nm pores. Although the parabolic polynomial approximation is only applicable to the section [0, z_0] in Figure 6 rather than [0, w], the upper bound of the outer integration in Eq. 6 is z_0, indicating the inactive nature of the zone [z_0, w] in the viscous model. Consequently, one only needs to investigate the characteristics of the potential energy profile in the zone [0, z_0] to develop the following simplified equation from Eq. 6:

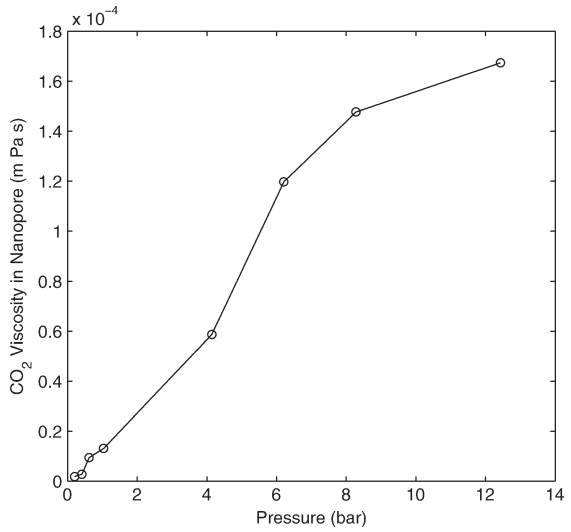

Figure 7. Viscosity variation with pressure in 1.5 nm graphite pore from MD simulations.

$$\begin{aligned} I &= \int_0^z \exp\left[-\frac{\Phi(\xi,w;p)}{k_B T}\right]d\xi = \int_0^z \exp\left[-\frac{a\xi^2+b}{k_B T}\right]d\xi \\ &= \exp\left(-\frac{b}{k_B T}\right)\left[-\frac{i\sqrt{\pi}}{2}\mathrm{erf}\left(iz\sqrt{-\frac{a}{k_B T}}\right)\right] \end{aligned} \tag{7}$$

where "erf" denotes the error function. As a result, the viscous and total diffusivities can be estimated using a much more tractable equation given by:

$$\begin{aligned} D_v &= \frac{(k_B T\rho_g)^2\pi}{4a\hat{\rho}\hat{\eta}w}\exp\left(-\frac{2b}{k_B T}\right)\int_0^{z_0}\left[\mathrm{erf}\left(iz\sqrt{\frac{a}{k_B T}}\right)\right]^2 dz \\ D_t &= D_s + D_v \end{aligned} \tag{8}$$

In this work, the error functions for complex numbers are computed using the computer codes provided by Leuteneger.[31] It should be noted that both "a" and "b" are pressure dependent with "b" [intersection $\Phi(0)$] being more sensitive to pressure variation. Adjustments of these two parameters can easily be incorporated in computations.

Equations 4 and 8 are the simplified tractable models developed in this work.

The average viscosity $\hat{\eta}$ is one of the outputs from GCMC simulations. The general trend of the viscosity variation of CO_2 with pressure at 300 K in 1.5 nm graphite pores is shown in Figure 7.

Both self and total diffusion coefficients obtained from MD simulations and computed using Eqs. 4 and 8 for CO_2 at 300 K are shown in Figure 8. It can be seen that the simple tractable models provide reasonable estimations. Using the simpler tractable models, a large number of simulations have been carried out over a wide range of conditions; in no case was CO_2 diffusivity higher than for CH_4.

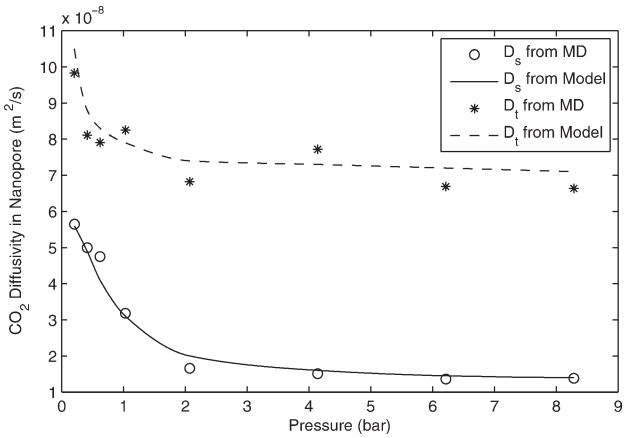

Figure 8. Comparison of MD simulation and tractable model prediction.

Kinetic Mobility and Connectivity

In this section, we demonstrate that larger diffusivity does not necessarily lead to larger molar flux, since other limiting mechanisms may be at play. First of all, molecules must pass through a large number of joints in pore networks. These joints can be considered as "gates" with different energy barriers for different gases. In the case that the effective gate opening is about 0.38 nm ($h = 0.38 + 0.34 = 0.72$ nm), the energy barrier (or equivalently, the activation energy) of CH_4 may be much larger than that of CO_2.

To estimate activation energies, we follow the work reported by Nguyen and Bhatia recently using MD simulations.[32] The desorption crossing time τ_d and rate constant k_d are given by:[32]

$$\begin{aligned} \tau_d &= b\sqrt{\frac{2\pi m}{k_B T}}\exp\left(\frac{E_d}{k_B T}\right) \\ k_d &= 1/\tau_d \end{aligned} \tag{9}$$

where b is a width parameter suggested to be 0.1 Å by Nguyen and Bhatia, E_d is the activation energy of desorption, and m is the molecular weight. In the computation of the activation energy E_d, we define the following two spaces: (1) the cage containing the adsorbed gas for desorption process, and (2) the box containing the dividing surface separating two pores. The activation energy consists of the contributions from these two spaces, which is estimated as follows:[32]

$$\begin{aligned} E_d &= \langle \phi_{sf} \rangle_b + k_B T \ln\left\{\sum_{i=1}^{n}\exp\left[-\frac{\phi_{sf}(\mathbf{r}_i)}{k_B T}\right]\right\} \\ n &\approx \frac{V_c}{V_b} \end{aligned} \tag{10}$$

In Eq. 10, $\langle \phi_{sf} \rangle_b$ stands for the average solid-fluid interaction potential in the box containing the dividing surface, $\phi_{sf}(\mathbf{r}_i)$ is the interaction potential between fluid molecule at coordinate $\mathbf{r}_i$ and all solid atoms of the adsorbent phase in the desorption cage, V_c and V_b are the volumes of the cage and box, respectively, and n is the number of grid points in the cage. The activation energy E_d for CH_4 and CO_2 desorption are computed as about 90 and 65 kJ/mol, respectively, which are reasonably consistent with the work reported by Nguyen and Bhatia.[32]

An example is explained here to illustrate the use of the activation energy. Suppose two 10 mm long, 1.0 nm nanopores are connected by a narrower throat with a width of 0.72 nm. The initial adsorbed concentration in both of the connected pores is specified as 1100 mol/m^3. The concentrations of the two ends are step changed to 1600 and 600 mol/m^3, respectively, and kept at these two boundary values throughout the operation. In this case, two submodels, applying to the sections on either side of the throat, may be developed as follows:

Section 1

$$\frac{\partial C_{\mu 1}}{\partial t} = D_{\mu 1}\frac{\partial^2 C_{\mu 1}}{\partial x^2}$$

initial and boundary conditions :

$$\begin{aligned} C_{\mu 1}(x,0) &= 1100\ \text{mol/m}^3,\ \text{as}\ t = 0,\ \forall x \\ C_{\mu 1}(0,t) &= 1600\ \text{mol/m}^3,\ \text{as}\ x = 0,\ t > 0 \\ -D_{\mu 1}\frac{\partial C_{\mu 1}(L,t)}{\partial x} - \delta_i k_d C_{\mu 1}(L,t) &= 0,\ \text{as}\ x = L,\ t > 0 \end{aligned}$$

Section 2

$$\frac{\partial C_{\mu 2}}{\partial t} = D_{\mu 2}\frac{\partial^2 C_{\mu 2}}{\partial x^2}$$

initial and boundary conditions :

$$\begin{aligned} C_{\mu 2}(x,0) &= 1100\ \text{mol/m}^3,\ \text{as}\ t = 0,\ \forall x \\ \delta_i k_d C_{\mu 1}(L,t) + D_{\mu 2}\frac{\partial C_{\mu 2}(L,t)}{\partial x} &= 0,\ \text{as}\ x = L,\ t > 0 \\ C_{\mu 2}(2L,t) &= 600\ \text{mol/m}^3,\ \text{as}\ x = 2L,\ t > 0 \end{aligned} \tag{11}$$

where δ_i is the component dependent film thickness with $i = 1$ and 2 for CH_4 and CO_2, respectively, $L = 0.01$ m is the length of each nanopore. Simulation results depicted in Figure 9 shows the gradual development and enlargement of the

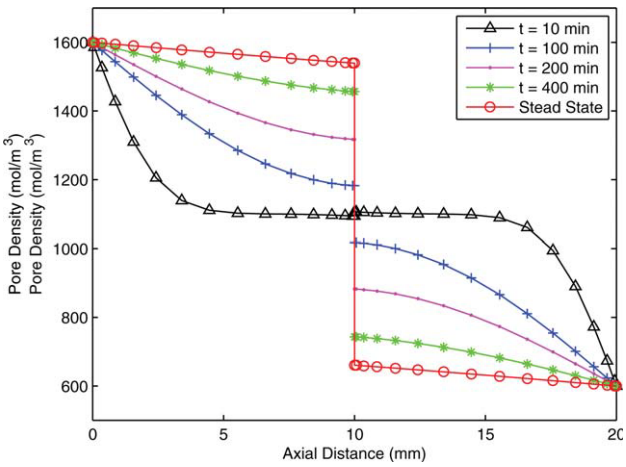

Figure 9. Development and enlargement of discontinuity near narrow throat.

[Color figure can be viewed in the online issue, which is available at wileyonlinelibrary.com.]

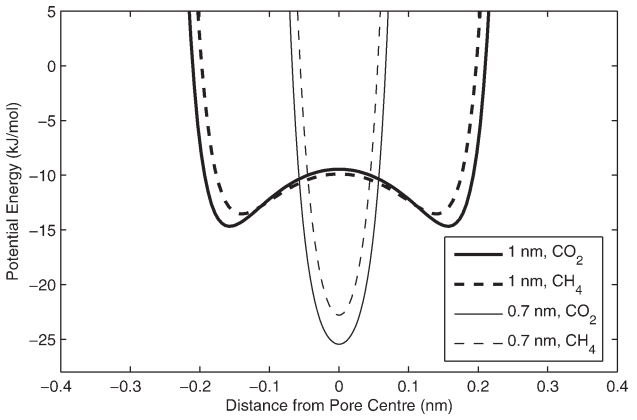

Figure 10. Potential energy profiles for CO_2 and CH_4 in 0.7 and 1.0 nm nanopores.

discontinuity with time near the throat from the originally continuous profile. However, the concentration must be first and second order differentiable for Fick's first and second diffusion laws to be valid. If E_d is large enough, this leads to a very small k_d as well as a very small molar flux given by $J = \delta_t k_d C_\mu(L,t)$ at steady state, and the "gate" can be considered as closed in practice. The concentration profile at final steady state is also shown in Figure 9. An overall diffusivity for systems with interior energy jumps can be seen to violate the continuity condition required for the validity of the conventional diffusion equation, losing generality and physical meaning.

In addition to activation energies generated by narrow throats, another relevant issue is the possible existence of directional force fields induced by nanopore geometries and compositions.[13] The directional forces can be accounted for using the Fokker-Planck or Smoluchowski diffusion equations developed from the Langevin equation given by:

$$\begin{aligned} m\ddot{\mathbf{x}} &= -\gamma\dot{\mathbf{x}} + \mathbf{F}(\mathbf{x}) + \sigma E(t) \\ \mathbf{x} &= \begin{bmatrix} x_1 \\ x_2 \\ \vdots \\ x_N \end{bmatrix};\ \mathbf{F} = \begin{bmatrix} F_1(\mathbf{x}) \\ F_2(\mathbf{x}) \\ \vdots \\ F_N(\mathbf{x}) \end{bmatrix} \end{aligned} \tag{12}$$

In Eq. 12, we assume that there are N molecules in the system; $\mathbf{x}$ and $\mathbf{F}$ are position and force vectors with x_1, …, x_N and F_1, …, F_N representing the positions and directional forces for individual molecules numbered from 1 to N; E is the random force; m is the mass of molecules; γ and σ are the frictional coefficient and amplitude of the random fluctuating force, respectively.

With the assumption that

$$|\gamma\dot{\mathbf{x}}| >> |m\ddot{\mathbf{x}}| \tag{13}$$

The following Fokker-Planck diffusion equation can be developed from Eq. 12:

$$\begin{aligned} \frac{\partial}{\partial t}C &= \left(\nabla^2 D - \nabla\cdot\frac{\mathbf{F}}{\gamma}\right)C \\ D &= \frac{\sigma^2}{2\gamma^2} \end{aligned} \tag{14}$$

If we further assume that the force field can be related to a scalar potential U given by:

$$\mathbf{F}(\mathbf{x}) = -\nabla U(\mathbf{x}) \tag{15}$$

The Fokker-Planck diffusion equation described by Eq. 14 can be converted to the Smoluchowski diffusion equation described as:

$$\begin{aligned} \frac{\partial}{\partial t}C &= \nabla\cdot[D(\nabla - \beta\mathbf{F})C] \\ &= \nabla\cdot[D(\nabla + \beta\nabla U)C] \\ \beta &= \frac{1}{k_B T} \end{aligned} \tag{16}$$

Since the potential energy U is a function of pore size and composition, Eq. 15 is nonzero if pore size or composition varies. The potential energy profiles for CO_2 and CH_4 in 0.7 and 1.0 nm nanopores are depicted in Figure 10. The computation is based on the single-center model with the parameters of CO_2 and CH_4 proposed by Ravikovitch et al.[27] and Bird et al.,[28] respectively (Table 1). From Figure 10, it can be seen that the potential energy wells of CO_2 are deeper than that of CH_4 in both pores. Although the absolute value of potential energy of CO_2 is normally higher than that of CH_4, the potential energy gradient could be the reverse. For example, profiles of the adsorption energy E of CH_4 and CO_2, defined as the negative value of the minimum potential energy, are shown in Figure 11 using the same parameter set as used for the development of Figure 10. Figure 11 shows that the difference of adsorption energy E of CH_4 in 0.8 and 1.0 nm pores is notably larger than that of CO_2 under the same conditions, leading to the larger directional force imposed on CH_4.

From Eq. 16, the condition for the existence of the molar flux in the positive direction is represented as:

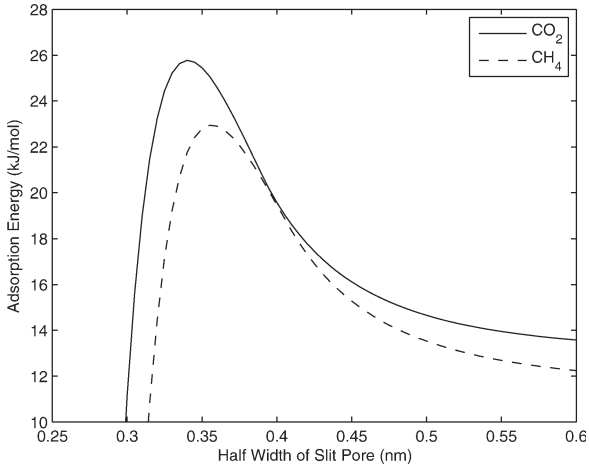

Figure 11. Adsorption energy variations of CO_2 and CH_4 with pore sizes.

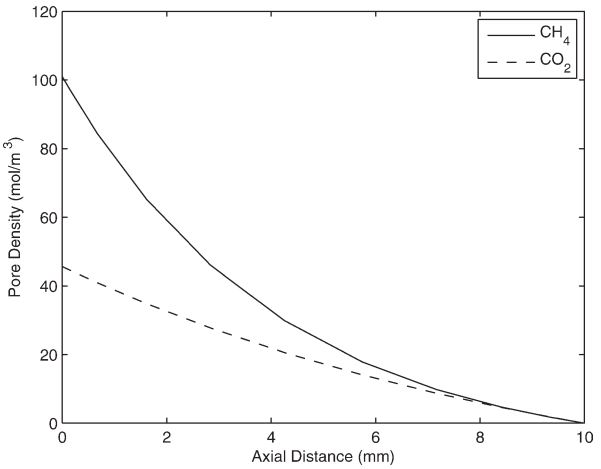

Figure 12. Concentration profiles for CO_2 and CH_4 in conic shaped pores with zero fluxes.

$$J = -D\nabla C - DC\beta\nabla U > 0$$
$$\nabla U < -k_B T\frac{\nabla C}{C} = -k_B T\nabla\ln(C) \quad (17)$$

In the case that $J = 0$, that is, $\bigtriangledown U = -k_B T \times \bigtriangledown \ln(C)$, no molar flux can be observed even for a nonzero concentration gradient $\bigtriangledown C$. If a 10 mm long cone-shaped graphite pore with small and large ends specified as 0.8 and 1.0 nm, respectively, is used for gas transport in the small end to large end direction, the CO_2 and CH_4 fluxes vanish with the profiles shown in Figure 12 based on the Smoluchowski diffusion equation. It can be shown that compared with CO_2, CH_4 requires much larger concentration gradient (more than twice) to achieve nonzero flux. This implies that conditions may occur, in which pores allowing CO_2 transport, may block CH_4 molecules due to different directional forces induced by different axial potential gradients.

This section has shown that (in contrast to fluid flow in large pores) molecular transport may be prevented in nanopores even if they have no physical blockage. The gate activation energy and the operation of ordered force fields on diffusion are identified as two major mechanisms that can lead to dramatically reduced mobility and connectivity. Further, these mechanisms act differently on different molecules and (under appropriate circumstances) may allow heavier molecules with larger attractive force to move more quickly through a pore network than lighter ones with smaller attractive force. This is exemplified by CO_2 and CH_4 transport through nanosized graphite pores, where the apparent transport coefficient of CO_2 is higher, relative to CH_4, even though its diffusion coefficient is smaller. It is important to distinguish apparent transport coefficients (which lump many transport properties) from diffusion coefficients, which have definite physical meaning.

Percolation Analysis of Nanopore Networks

In previous sections, transport properties of single pores with uniform and variable pore sizes were analyzed using both MD simulations and fast predictions based on simplified, tractable models. In this section, we consider networks of pores, analyzed using graph and set theory applied to percolation. Probabilistic modeling strategies incorporating kinetic mobility and connectivity are then used to assess the characteristics of interconnected pore systems.

Percolation theory describes the characteristics of connected clusters in a random network consisting of spatially associated vertices and edges. In graph theory, a graph represented by $G = (\mathbf{V}, \mathbf{E})$ consists of vectors of vertices and edges denoted by $\mathbf{V}$ and $\mathbf{E}$, respectively. From a physical perspective in the system under consideration here, edges represent all possible pores and vertices represent possible points of connection of the pores. In addition to percolation theory,[14–17] fundamental background knowledge on graph theory[33,34] is also required for the current study. For clarity, we recite some definitions.

Probability of occupied edges[23,35] denoted by P, also named as occupation probability for simplicity, is the fraction of the number of the occupied edges over the total edge number. "Occupied" edges are those open for fluid flow, although they may not be all active. Examples of occupied but inactive edges are those that are isolated from other occupied edges or where the kinetic energy of molecules in edges is insufficient to overcome the energy barriers and/or the directional forces opposing transport.

A "spanned cluster"[23,35] is the collection of all interconnected edges, which spans the complete space. For example, in a coal system, this may represent the matrix porosity network that connects to and allows flow of methane from the body of the coal to the cleats. In this work, we have focused on spans across the x–y plane but not in the z-direction. This corresponds to the practical situation in many cases, for example, fluid in a natural geological reservoir may flow horizontally but be restricted by impermeable ply layers from flowing vertically.

"Percolation threshold"[14–17] is the critical probability P_c for the formation of long-range connectivity in a random network. When the occupation probability P passes the percolation threshold ($P \geq P_c$), there are connected paths which span the complete space.

"Shortest representative path"[23] in each spatial direction satisfy the following three conditions in the respective direction: (1) spanning the complete length; (2) closest to the central axis; and (3) with shortest length. (Choosing the span closest to the central axis simply provides a convenient rule for selecting a representative path that is unlikely to dead-end against a side boundary.)

"Tortuosity factor"[36] τ is usually defined as $\tau = (L_e/L) \geq 1$, where L is the length of a straight line connecting both ends of the tortured length, L_e. For a complex pore network involving many pores and paths, a unique representation of the tortuosity factor does not exist. We propose a strategy for estimating a value of the tortuosity factor for a network, denoted by τ_M, which will be described later.

"Network length"[23] L is a dimensionless parameter defined as $L = L_m/\iota$, where L_m and ι denote the metric network length and a single pore length, respectively (both with the metric unit m). Consequently, the 3D network lengths L_x, L_y, and L_z are measured by the numbers of unit pores in x, y, and z directions. This definition is applied to the network representation and analysis in this article.

Rigorously speaking, "edge" defined in the graph theory is different from "pore" defined in engineering applications with the former to be more structuralized and standardized.

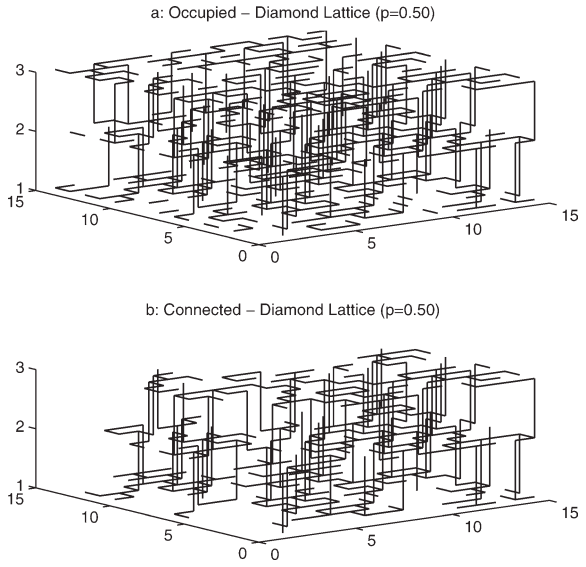

Figure 13. Occupied and connected pores in 3D diamond lattice with $P = 0.50$. Dimensionless network size.

To avoid additional complexity, we do not distinguish both in this article. Since pores in porous media can be mapped to the edges in the network graphs, this approximation will not lead to conceptual confusion.

A percolation analysis consists of the following steps: (1) Construction of the two-dimensional (2D) or three-dimensional lattices; (2) Evaluation of edge widths based on specified size distributions; (3) Determination of occupied and connected pores; (4) Evaluation of spanned and shortest representative path; and (5) Characterization of overall pore network in terms of percolation threshold, tortuosity factor, and effective porosity. We use a graph theory package associated with MATLAB,[37] namely matlab_bgl,[38] which is a set of MATLAB wrappers for the Boost Graph Library.

Only networks of quite limited complexity are presented here, with a view to demonstrate the concepts and to show that the method provides useful insights about experimental transport observations. The graph theory approach to percolation using the software packages in MATLAB permits easy integration into a unified framework for network analysis, but it may not be effective for large networks, which require more effective algorithms, for example, Knackstedt et al.[35]

In this work, 3D diamond and hybrid cube-diamond lattices are used for the representation of nanopore networks in coals. Physically, this represents a vertex with three connecting pores, or one pore butting into another in the x–y plane.

Occupied and connected pores in a 3D diamond lattice are shown in Figures 13a,b, respectively, for the case when the specified occupation probability $P = 0.5$. The computed percolation threshold is about $P_c = 0.45$. Comparing Figure 13a, which shows all of the occupied pores, with Figure 13b, from which isolated pores are removed, it is apparent that connected pores are very important to percolation analysis. Furthermore, some proportion of the pores in Figure 13b may be kinetically inactive (due to large energy barriers and strong directional forces) and should in principle also be removed.

Since methane experiences larger activation energy and/or stronger directional forces than CO_2, there will consequently be a larger proportion of pores inactive to CH_4 transport compared with CO_2. If an additional 12 and 6% pores are deleted from Figure 13a (as an example) to account for inactive pores for CH_4 and CO_2 transport, respectively, CH_4 percolation will stop entirely since $P < P_c = 0.45$, whereas CO_2 percolation continues since for CO_2 $P > P_c$, although at a reduced rate. In this case, the flux ratio between CO_2 and CH_4 approaches infinity, that is, $J_{CO2}/J_{CH4} \rightarrow \infty$.

In addition to the percolation threshold, another important issue in percolation analysis is the tortuosity. It is relatively easy to define tortuosity for a single path, but for complex pore networks consisting of multiple paths, there is no simple representation. We propose a convenient estimate of the tortuosity factors for a network, denoted by τ_{M0} and τ_M as follows:

$$\begin{aligned} \tau_{M0} &= \frac{n_{sp\_t}}{\left(w_{min\_x}L_x + w_{min\_y}L_y\right)} \\ w_{min\_x} &= \min\left\{n_{spc\_x}(x)\right\},\ \forall x \\ w_{min\_y} &= \min\left\{n_{spc\_y}(y)\right\},\ \forall y \\ \tau_M &= \frac{\tau_{M0}}{\left(\frac{\varepsilon_e}{\varepsilon}\right)} \\ \frac{\varepsilon_e}{\varepsilon} &= \frac{V_{sp\_p}}{V_p} \end{aligned} \tag{18}$$

where, τ_M and τ_{M0} represent tortuosity factors with and without accounting for porosity effect, respectively, n_{sp_t} is the total number of pores in the spanned cluster, $n_{spc\_x}(x)$ is the numbers of pores in the spanned cluster, which cross the plates perpendicular to x-axis at the locations x, $n_{spc\_y}(y)$ is defined in the similar way as $n_{spc\_x}(x)$ for pores along y-direction, w_{min_x} and w_{min_y} are the minimum numbers of pores in the spanned cluster crossing the plates perpendicular to x- and y-directions, respectively, ε_e and ε are effective and total porosity, respectively, V_{sp_p} and V_p are the volumes of pores in the spanned cluster and in the whole specimen, respectively. For convenience (since this does not require pore widths or system void fractions) we also define simple lower and upper bounds of tortuosity factor for the shortest and longest representative paths, denoted by τ_L and τ_U, respectively, as follows:

$$\begin{aligned} \tau_L &= \frac{\left(n_{sh\_x} + n_{sh\_y}\right)}{\left(L_x + L_y\right)} \\ \tau_U &= \frac{\left(n_{max\_x} + n_{max\_y}\right)}{\left(L_x + L_y\right)} \end{aligned} \tag{19}$$

where n_{sh_x} and n_{sh_y} are the numbers of pores in the shortest representative paths conducting x- and y-direction flows, respectively, n_{max_x} and n_{max_y} denote the numbers of pores in the longest representative paths conducting x- and y-direction flows, respectively, in the representative spanned cluster. It should be noted that it is possible for τ_U to be less than τ_M as a result of effects from porosity and path overlaps despite its definition as the tortuosity factor for the longest representative path.

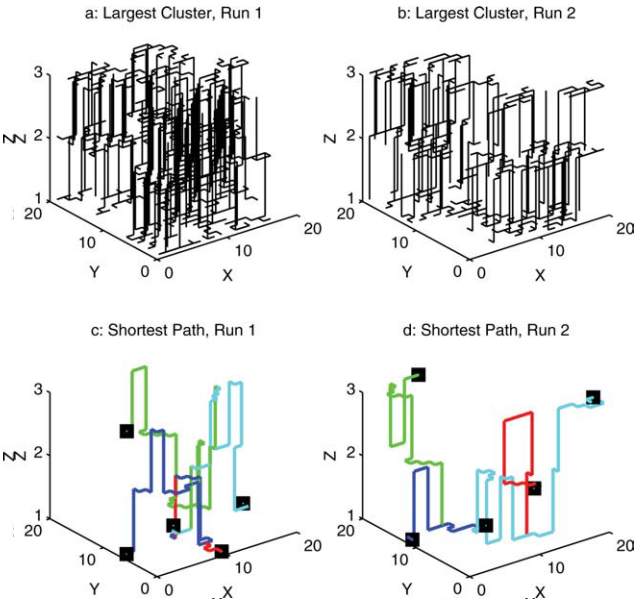

Figure 14. Illustrative networks of largest cluster and shortest path in two simulations for a 3D diamond lattice with $P = 0.48$. Dimensionless network size.

[Color figure can be viewed in the online issue, which is available at wileyonlinelibrary.com.]

From Eq. 19, one can make the following two important observations: (1) for 2D triangle and square, and for 3D cube lattices, $\tau_L = 1$ as $P = 1$; however, $\tau_L > 1$ for other lattices in all circumstance; and (2) the tortuosity factors vary over a very broad range, possibly deviating by one or two orders of magnitude from nominal values.

Results from two different simulations for a thin specimen ($L_z = 3$) are shown in Figure 14. In the first run, the value of r_e defined as the ratio between spanned and total pore numbers n_s/n_t is 0.32, with outcomes are depicted in Figures 14a,c. In the second run a lower r_e value (0.20) was obtained, with outcomes shown in Figures 14b,d. The difference in the values for r_e arises from the use of statistical (probabilistic) methods, which provide different results for each simulation even with the same model inputs. In spite of the nonuniqueness of the solutions, general trends can be developed and these provide important implications, in particular, the provision of the information on tortuosity. Although two different r_e values are obtained for the thin specimens, both values are notably larger than that for the thick specimen due to the reduced contributions from vertical pores to the connectivity in x–y direction. We will extend this simple analysis to a larger network population in a later article.

From Figure 14, it can be seen that near the percolation threshold, the values of tortuosity are quite high. The lower bounds of the tortuosity τ_L are in the range of 3.0–4.0, whereas the tortuosity factor τ_M, defined by Eq. 18, varies in a very broad range from 20 to 65 for the same lattice, as obtained from the results of a number of simulations. When a larger lattice (e.g., $50 \times 50 \times 10$ diamond lattice) is simulated, τ_M could be higher than 100. This justifies the statement that it is difficult to define a unique tortuosity factor for complex pore networks as commonly treated in porous media operations. Another important observation from Figure 14 is that in the first run (Figures 14a,c) we obtain $r_e = 0.32$, $\tau_L = 3.12$, whereas for the second run $r_e = 0.20$, $\tau_L = 3.02$ (Figures 14b,d). It is easy to show that the higher the r_e value, the higher the effective porosity. This observation challenges the widely used Archie's law described by[17]

$$\frac{\varepsilon}{\tau} = \varepsilon^{\alpha} \tag{20}$$

where α is a parameter to be determined experimentally. Equation 20 leads to monotonic decrease of the tortuosity with the increase of the porosity. This has important practical consequences and further work along this line is necessary to gain an appreciation of the implications.

The shortest path and tortuosity also change significantly with types of lattices in addition to the occupation probability. The shortest path of a cube lattice is significantly smaller than that of diamond lattice with the same occupation probability as shown in Figure 15, indicating a smaller tortuosity.

The way the lower bound of tortuosity factor, τ_L, defined in Eq. 19 as a dimensionless parameter, varies with probability of occupied pores for three different lattices, namely cube, diamond and hybrid lattices, are shown in Figure 16. Three clear trends may be identified: (1) Tortuosity factor τ_L of diamond lattice is notably higher than that of hybrid and cube lattices; (2) Tortuosity factor reduces dramatically with the increase of the occupation probability (that is, as the number of active pores increases); and (3) The lower bound of the tortuosity factor for diamond lattice is always significantly greater than one. The same trends are also true for the values of the tortuosity factors τ_M and τ_U, and these have much higher numerical magnitudes.

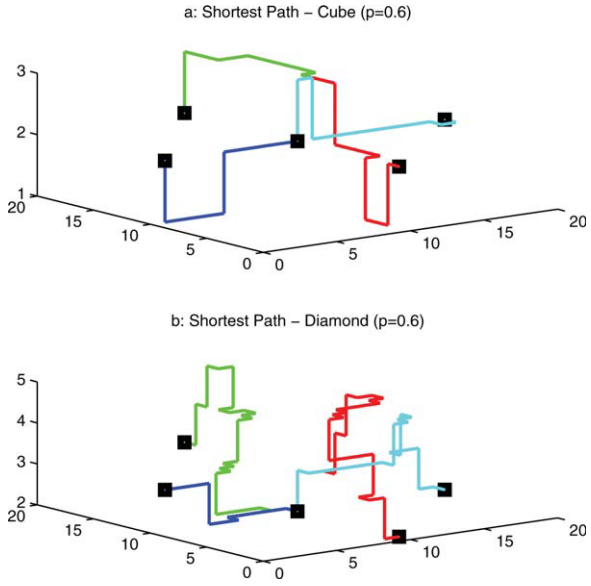

Figure 15. Shortest paths for cube and diamond lattices with $P = 0.60$. Dimensionless network size.

[Color figure can be viewed in the online issue, which is available at wileyonlinelibrary.com.]

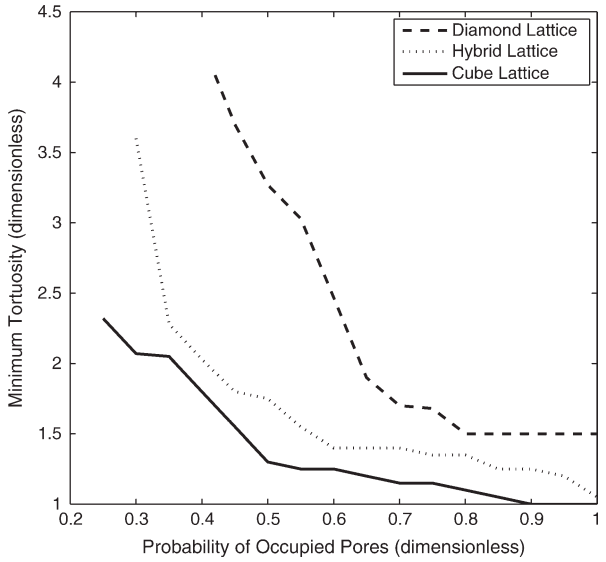

Figure 16. Variations of tortuosity with probability of occupied pores for three lattices.

We consequently put forward the argument that it is the occupation probability (proportional to the number of active pores) and/or lattice type which results in significant variations in tortuosity, and this partly explains the higher mobility of CO_2 over CH_4, even though the diffusivity of CO_2 is much lower. For example, if CO_2-graphite and CH_4-graphite systems are represented by cube-diamond hybrid lattice and pure diamond lattice, respectively, the tortuosity factor of the former could be an order of magnitude smaller than the latter, leading to much lower CH_4 transport compared with CO_2, as often experimentally observed, without violating conventional diffusion theory.

For engineering approximations, the component dependent tortuosity factor and porosity can be incorporated with diffusion into a transport model as follows:

$$\frac{\partial C_i}{\partial t} = \frac{\partial}{\partial x}\left(k_i \frac{\partial C_i}{\partial x}\right) \qquad k_i = \frac{\varepsilon_{ei}}{\varepsilon}\frac{D_i}{\tau_{\mathrm{M0}\_i}} \tag{21}$$

where ε_e and ε are effective and total porosity, respectively, and the subscript i indicates the species. It is now apparent that under certain conditions, $k_{CO_2} > k_{CH_4}$ even though $D_{CO_2} < D_{CH_4}$ provided that the values for ε_e are suitably large and/or the values for τ_{M0} are suitably small for CO_2, as percolation analysis shows may demonstrably be the case. However, although it is possible to fit the experimental data by adjusting the component dependent tortuosity factor and effective porosity in Eq. 21, this engineering approach cannot accurately predict the internal concentration distributions, in particular profiles with discontinuities, due to poor understanding of other important mechanisms. Consequently, its applications should be restricted to rough engineering estimations. More rigorous analysis proposed in this work is necessary if the detailed concentration profiles are required.

Conclusions

Through comprehensive simulations using GCMC, MD and simplified (tractable) models developed in this work, coupled with pore network analysis based on percolation theory, the following conclusions can be drawn.

(1) Both of the self and total diffusion coefficients of CO_2 in graphite nanopores are significantly smaller than that of CH_4 under a broad range of practical operational conditions. Contradictory trends reported in the literature were most likely obtained for processes constrained by other mechanisms, leading to the development of "apparent transport coefficients" not true diffusivities. The proper definition of diffusivity relies upon tightly constrained underlying mathematical assumptions.

(2) The tractable models derived in this article using the integral mean value theorem and parabolic approximations together with the total potential energy to account for all possible interactions in nanopores provide a technique for fast computations of diffusivity with acceptable accuracies. The tractable models are structurally consistent with commonly used empirical models, but theoretically more rigorous. This provides physical explanations for some of the empirical equations often used in current practice.

(3) Kinetic mobility and connectivity for systems with large energy barriers and directional force fields induced by narrow molecular entrances and nonuniform geometries show that CH_4 molecules need to overcome much higher energy barriers than CO_2 for passing through narrow throats with the sizes near the CH_4 kinetic diameter. Furthermore, larger directional forces can be imposed on CH_4 molecules in the pore size range 0.8–1.0 nm due to larger potential energy gradients. Pores and joints between pores that may permit transport of CO_2 may not be active for CH_4 transport. What constitutes a spanned cluster for one species in conventional percolation analysis may not be fully active for another species.

(4) A graph theory approach to pore network analysis has been presented, which incorporates kinetic mobility and connectivity considerations. Near the percolation threshold, transport is particularly sensitive to the remaining active pores. If more pores from the CH_4-graphite network become inactive than from the corresponding CO_2-graphite network, then the relative fluxes of CO_2 and CH_4 may change dramatically and in opposition to their relative diffusivities. Experimental observations of faster CO_2 transport relative to CH_4 can then be explained quantitatively and in a physically plausible way. In practice, the effects of kinetic mobility and connectivity on network percolation can be evaluated approximately by introducing time and component dependent tortuosity factors and effective porosities.

Acknowledgments

The authors thank Professor David Nicholson for his professional help and valuable discussions on GCMC and MD simulations. The financial support from Australian Research Council (ARC) is also gratefully acknowledged.

Literature Cited

1. Cui XJ, Bustin RM, Dipple G. Selective transport of CO2, CH4 and N2 in coals: insights from modelling of experimental gas adsorption data. *Fuel*. 2004;83:293–303.

2. Shi JQ, Durucan S. A bidisperse pore diffusion model for methane displacement desorption in coal by CO2 injection. *Fuel*. 2003;82:1219–1229.
3. Wei XR, Wang GX, Massarotto P, Rudolph V. Numerical simulation of multi-component gas diffusion and flow in coals for CO2 enhanced coal-bed methane recovery. *Chem Eng Sci*. 2007;62:4193–4203.
4. Wang FY, Zhu ZH, Massarotto P, Rudolph V. A simplified dynamic model for accelerated methane residual recovery from deep coals. *Chem Eng Sci*. 2007;62:3268–3275.
5. Wang FY, Zhu ZH, Massarotto P, Rudolph V. Mass transfer in coal seams for CO2 sequestration. *AIChE J*. 2007;53:1028–1049.
6. Bhatia SK, Nicholson D. Hydrodynamic origin of diffusion in nanopores. *Phys Rev Lett*. 2003;90:016105-1–016105-4.
7. Bhatia SK, Nicholson D. Molecule transport in nanopores. *J Chem Phys*. 2003;119:1719–1730.
8. Potoff J, Siepmann J. Vapor-liquid equilibra of mixtures containing alkanes, carbon dioxide and nitrogen. *AIChE J*. 2001;47:1676–1682.
9. Do DD, Do HD. Adsorption of carbon tetrachloride on graphitized carbon black and in slit graphitic pores: Five-site versus one-site potential models. *J Phys Chem B*. 2006;110:9520–9528.
10. Do DD, Do HD. Adsorption of benzene on graphitized carbon black: Reduction of the quadrupole moment in the adsorbed phase. *Langmuir*. 2006;22:1121–1128.
11. Steele WA. *The Interaction of Gases with Solid Surface*. Oxford: Pergamon, 1974.
12. Reid RC, Prausnits JM, Poling BE. *Properties of Gases and Liquids*, 4th ed. New York: GcGraw-Hill, 1987.
13. Wang FY, Zhu ZH, Rudolph V. Diffusion through ordered force field in nanopores represented by Smoluchowski equation. *AIChE J*. 2009;55:1325–1337.
14. Sahimi M. *Application of percolation Theory*. London: Taylor & Francis, 1994.
15. Hunt AG. *Percolation Theory for Flow in Porous Media*. Berlin: Springer, 2005.
16. Dullien FAL. *Porous Media: Fluid Transport and Pore Structure*, 2nd ed. San Diego: Academic Press, 1992.
17. Sahimi M. *Flow and transport in porous media and fractured rock: From classical methods to modern approaches*. Weinheim: VCH, 1995.
18. Seaton NA. Determination of the connectivity of porous solids from nitrogen sorption measurements. *Chem Eng Sci*. 1991;46:1895–1909.
19. Murray KL, Seaton NA, Day MA. Use of mercury intrusion data, combined with nitrogen adsorption measurements, as a probe of pore network connectivity. *Langmuir*. 1999;15:8155–8160.
20. Chen F, Mourhatch R, Tsotsis T, Sahimi M. Pore network model of transport and separation of binary mixtures in nanoporous membranes. *J Membr Sci*. 2008;315:48–57.
21. Hunt AG. Percolation theory and the future of hydrogeology. *Hydrogeology J*. 2005;13:202–205.
22. Hunt AG. Scale-dependent hydraulic conductivity in anisotropic media from dimensional cross-over. *Hydrogeology J*. 2005;14:499–507.
23. Kieling K, Rudolph T, Eisert J. Percolation, renormalization, and quantum computing with nondeterministic gates. *Phys Rev Lett*. 2007;99:130501(1–4).
24. Wang FY, Zhu ZH, Rudolph V. Molecular transport in nano-pores with broad size distribution. *AIChE J*. 2008;54:2009–2023.
25. Sun Y, Spellmeyer D, Pearlman DA, Kollman P. Simulation of the salvation free energies for methane, ethane and propane and corresponding amino acid dipeptides: A critical test of the "Bond-PNF" correction, a new set of hydrocarbon parameters and the gas phase-water hydrophobicity scale. *J Am Chem Soc*. 1992;114:6798–6801.
26. Do DD, Jumpirom D, Nicholson D, Do HD. Importance of molecular shape in the adsorption of nitrogen, carbon dioxide and methane on surfaces and in confined spaces. *Colloids Surf A*. 2010;353:10–29.
27. Ravikovitch PI, Vishnyakov A, Russo R, Neimark AV. Unified approach to pore size characterization of microporous carbonaceous materials from N2, Ar and CO2 adsorption isotherms. *Langmuir*. 2000;16:2311–2320.
28. Bird RB, Stewart WE, Lightfoot EN. *Transport phenomena*, 2nd ed. New York: John Wiley, 2002.
29. Jepps OG, Bhatia SK. Modeling molecule transport in slit pores. *J Chem Phys*. 2004;120:5396–5406.
30. Bae J-S, Do D.D. Permeability of subcritical hydrocarbons in activated carbon. *AIChE J*. 2005;51:487–501.
31. Leutenegger M. Error function of complex numbers. Available at: http://www.mathworks.com/matlabcentral/fileexchenge/18312; Updated January 14, 2008.
32. Nguyen TX, Bhatia SK. Kinetic restriction of simple gases in porous carbon: Transition-state theory study. *Langmuir*. 2008;24:146–154.
33. Marshall CW. *Applied graph theory*. New York: Wiley-Interscience, 1971.
34. Trudeau RJ. *Dots and Lines*. Kent: The Kent State University Press, 1976.
35. Knackstedt MA, Sahimi M, Sheppard AP. Invation percolation with long range correlation: First-order phase transition and nonuniversal properties. *Phys Rev E*. 2000;61:4920–4934.
36. Epstein N. On tortuosity and the tortuosity factor in flow and diffusion through porous media. *Chem Eng Sci*. 1989;44:777–779.
37. MATLAB 7.7. The Math Works, 2008.
38. Gleich D. MatlabBGL 4.0, A Matlab Graph Library. Available at: http://www.stanford.edu/~dgleich/programs/matlab_bgl/; Updated 22 October 2008.

Manuscript received Oct. 15, 2010, and revision received Jan. 23, 2011.